Science in China Series E: Technological Sciences

www.scichina.com
tech.scichina.com
www.springerlink.com

Seismic damage-cracking analysis of arch dams using different earthquake input mechanisms

PAN JianWen, ZHANG ChuHan†, WANG JinTing & XU YanJie

State Key Laboratory of Hydroscience and Engineering, Tsinghua University, Beijing 100084, China

In this study, a nonlinear model is presented for analysis of damage-cracking behavior in arch dams during strong earthquakes using different seismic input mechanisms. The nonlinear system includes a plastic-damage model for cyclic loading of concrete considering strain softening and a contact boundary model of contraction joint opening. Two different earthquake input mechanisms are used for comparison, including massless foundation input model and viscous-spring boundary model considering radiation damping due to infinite canyon. The results demonstrate that effects of seismic input mechanism and radiation damping on nonlinear response and damage-cracking of the dam are significant. Compared with the results of using massless foundation input model, the damage-cracking region and contraction joint opening are substantially reduced when using viscous-spring boundary model to take into account radiation damping. However, if the damping ratio of the dam is artificially increased to about 10%—15% for massless foundation input model, the joint opening and damage-cracking of the dam are comparable to the results obtained from the viscous-spring boundary model.

earthquake input mechanism, damage-cracking, radiation damping, contraction joints, arch dam

1 Introduction

In current design practice, the linear elastic theory is commonly used for earthquake resistance design of arch dams and the criteria of maximum principal stresses are adopted to evaluate safety factors of dams[1], where the nonlinear behavior of contraction joint opening and damage-cracking of the material are ignored. However, as a quasi-brittle material, concrete behaves as linear elastic only when it is subjected to limited normal loads, while damage-cracking will occur when the tensile stresses exceed the concrete strength during strong earthquakes. Therefore, in safety evaluation of a high arch dam during the maximum credible earthquake, it is necessary to assess the damage-cracking development and contraction joint opening in the dam.

The behavior of nonlinear contraction joint opening in arch dams during earthquakes has been studied for years[2−9]. However, few, if any, researches have touched the nonlinearity of concrete material, i.e. damage-cracking behavior of arch dams. Early studies of seismic cracking analysis mainly focused on gravity dams based on procedures of fracture mechanics[10−12], and the discrete crack model[11] for analysis of cracking development in concrete was a common approach. As an alternative procedure, the continuum method with a crack band model was also developed[13] for cracking study of gravity dams, which takes into account the strain softening behavior of concrete. The crack band model describes the crack as a band containing concentrated parallel fissures, while the material outside the crack band remaining linear elastic. This model replaces the isotropic constitutive relation with orthotropic properties in

Received May 16; accepted July 4, 2008; published online November 23, 2008
doi: 10.1007/s11431-008-0303-6
†Corresponding author (email: zch-dhh@tsinghua.edu.cn)
Supported by the National Natural Science Foundation of China (Grant Nos. 90510018, 90715041) and the National Basic Research Program of China ("973") (Grant No. 2002CB412709)

the failure zone. Once the concrete reaches its tensile strength, the material inside the crack band exhibits strain softening behavior and follows the corresponding softening constitutive relation. Some researchers have employed the crack band theory to model the failure of dams subjected to strong earthquake[14,15]. Recent developments using continuum damage mechanics to model nonlinear response of concrete dams[16] included consideration of inelastic (or plastic) strains for dilatancy control, which is important for modeling concrete structures under cyclic loading and unloading or multi-axial loading conditions. This is so-called the plastic-damage model proposed by Lubliner et al.[17]. The model uses one scalar damage variable based on fracture energy to represent damage states. Besides, the model introduces variables to describe the degradation of elastic stiffness. However, when coupled with plastic deformation in the constitutive relations, the degradation variables may cause some numerical instability problems. In addition, a single damage variable cannot appropriately simulate concrete structures subjected to cyclic loadings in several damage states. Thus, Lee and Fenves improved the plastic-damage model[18] by using two fracture-energy-based damage variables, one for tensile damage and the other for compressive damage, and a yield function with multiple damage variables to account for different damage states under cyclic loading. The constitutive relations for elastoplastic response are decoupled from the degradation damage response, leading to straightforward numerical implementation. The improved plastic-damage model was used to simulate the response of Koyna dam during 1967 Koyna earthquake[19], and it demonstrated that the model is capable of modeling failure process of the dam.

In this paper, a nonlinear system is presented to study contraction joint opening and damage-cracking in arch dams under strong earthquakes. This system combines three components: the plastic-damage model for simulating the damage-cracking behavior of concrete, the contact boundary model for joint opening, and the earthquake input mechanisms including massless foundation input model and viscous-spring boundary model considering radiation damping. Herein, firstly the accuracy of viscous-spring boundary model is verified. Secondly, the plastic-damage model and the contact boundary model are briefly introduced. Finally, as an engineering application the nonlinear response of the 210 m high Dagangshan arch dam subjected to the design earthquake with PGA of 0.557 g is evaluated. In addition, the results obtained from linear elastic material analysis were reported elsewhere and are cited herein for comparison.

2 Modeling of the system

This seismic nonlinear analysis of arch dams using finite element method includes three integrated components: modeling of damage-cracking of concrete, consideration of contraction joint opening, and the two different earthquake input models, i.e. massless foundation input model and viscous-spring boundary model. Herein, the three components of the system are briefly described.

2.1 Earthquake input mechanisms

It is a common practice to use a truncated foundation in the FE model for seismic analysis of arch dam-foundation system. Earthquake input mechanisms associated with the foundation models should ensure that the dynamic response of the dam-foundation system is objective. Thus, two earthquake input models are introduced and compared in this study, i.e. massless foundation input model and viscous-spring boundary model considering radiation damping due to infinite canyon.

The massless foundation input model was proposed by Clough[2] and has been used extensively in seismic analysis of concrete dams. It is assumed that the foundation is absence of mass, only the flexibility of the rock is considered. The specified free-field acceleration time history is applied uniformly at the truncated foundation base. Since the wave propagation velocity in the assumed massless rock approaches infinity, the input motions are transmitted instantaneously through the rock to the dam-foundation interface, and the motions at the interface is the same as the input one. It neglects the effects of radiation damping due to infinite canyon. However, the radiation effects significantly influence the response of arch dam-foundation system during earthquakes. The viscous boundary proposed by Lysmer and Kuhlemeyer[20] and the multi-transmitting boundary proposed by Liao et al.[21] are the two traditional non-reflecting boundaries for FE method to take into account the radiation effects, and this type of artificial boundary was later improved by other researchers[22,23]. In this study, a viscous-spring boundary model is employed for considering the radiation effects of the infinite canyon. This model is efficient and convenient to incorporate itself with current FE code and has sufficient accuracy

without much increasing computational efforts.

The viscous-spring boundary model is derived based on the free-field motions in a half-space assuming that waves are absorbed when reaching the truncated boundaries. For modeling this absorptive mechanism, pairs of springs and viscous dampers are installed at the truncated boundaries to satisfy the boundary conditions. Figure 1 shows an FE model with viscous-spring boundaries cut from the half-space. Normal and tangential springs and dampers are installed in the nodes of the truncated boundaries. The stiffness of springs and the coefficient of dampers are given as follows:

$$K_{l\mathrm{n}} = a_{\mathrm{n}} \cdot \frac{2G}{r}, \quad C_{l\mathrm{n}} = b\rho c_{\mathrm{P}}, \tag{1}$$

$$K_{l\mathrm{s}} = a_{\mathrm{s}} \cdot \frac{G}{2r}, \quad C_{l\mathrm{s}} = b\rho c_{\mathrm{S}}, \tag{2}$$

where subscript l is the node number on the truncated boundary; n and s refer to the normal and tangential directions of the boundary plane; G is the shear modulus; c_{P} and c_{S} denote the velocities of P and S waves respectively; ρ is the mass density; r is the distance from the wave source to the node l; a_{s}, a_{n} and b are modification coefficients, which may be determined from parameter analysis.

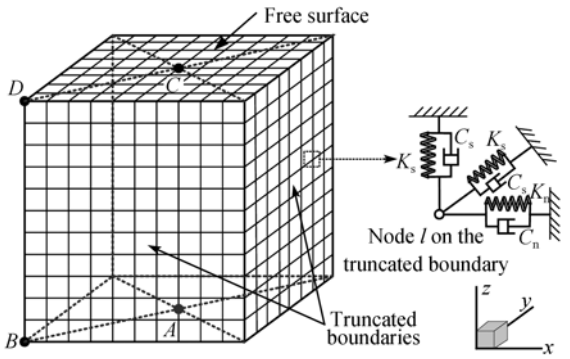

Figure 1 Sketch of the viscous-spring boundary model for square foundation.

The viscous-spring boundary is available for outgoing waves, but incident waves such as earthquake motion can not be directly input from the truncated boundaries. Herein, the incident wave motions are converted to equivalent tractions exerted on the truncated boundaries. For satisfying these displacement and traction conditions at the truncated boundaries due to the free field in half-space, the equivalent input force $\boldsymbol{f}_l(t)$ at the node l may be obtained as

$$\boldsymbol{f}_l(t) = \boldsymbol{K}_l \boldsymbol{u}_0(x_l, y_l, z_l, t) + \boldsymbol{C}_l \dot{\boldsymbol{u}}_0(x_l, y_l, z_l, t) + \boldsymbol{\sigma}_0(x_l, y_l, z_l, t), \tag{3}$$

where $\boldsymbol{u}_0(x_l, y_l, z_l, t)$ and $\dot{\boldsymbol{u}}_0(x_l, y_l, z_l, t)$ are the displacements and velocities of free field at node l; $\boldsymbol{K}_l$ and $\boldsymbol{C}_l$ are the stiffness and viscous coefficients of the springs and dampers at node l; $\boldsymbol{\sigma}_0(x_l, y_l, z_l, t)$ are the tractions at node l caused by the free field.

The first two terms on the right-hand side of eq. (3) are respectively the added elastic and damping forces to counteract those exerted on the truncated boundary by springs and dashpots. The third term represents tractions at the truncated boundaries due to the input waves which usually take one half values of the free-field motions on the ground surface by 1-D deconvolution.

Herein, an idealized square foundation is given to verify the feasibility of the viscous-spring boundary input model. A cubic region with a size of 500 m× 500 m×500 m is cut from the elastic half space, and discretized into two meshes of 8-node-brick elements with element size of 25 m×25 m×25 m and 15 m×15 m×15 m, respectively. The monitoring points A, B, C and D are shown in Figure 1. The shear modulus is $G = 1\times10^9$ Pa and the mass density is ρ=2000 kg/m^3. The propagation velocities of P-wave and S-wave are c_{P}=1224.7 m/s and c_{S}=707.1 m/s, respectively. In this case, r is set to be 500 m; the modification coefficients: a_{s}=1.3, a_{n}=0.6 and b=1.0.

The displacements of incident wave are defined as

$$\begin{aligned} u(\tau) = A_i[&16G(\tau) - 64G(\tau - 0.25) + 96G(\tau - 0.5) \\ &- 64G(\tau - 0.75) + 16G(\tau - 1)], \\ G(\tau) = \tau^3 H(\tau), &\quad \tau = t/T, \end{aligned} \tag{4}$$

where T is the time duration and in this analysis T=1 s; A_i are the amplitudes of the pulses in the three directions of x, y and z respectively. In this example, A_x=1.0 cm, A_y=0.75 cm and A_z=0.5 cm. $H(\tau)$ is the Heaviside function, defined as

$$H(\tau) = \begin{cases} 1, & \tau > 0, \\ 0, & \tau \leqslant 0, \end{cases} \tag{5}$$

The time histories of displacements and corresponding accelerations of incident waves are shown in Figure 2(a) and (b) respectively.

The acceleration responses in z direction at the free surface (responses in x and y directions are similar to that in z direction and not shown here for space limitation) are shown in Figure 3. The pulses are input from the bottom surface at the same time instant, i.e. t=0 s.

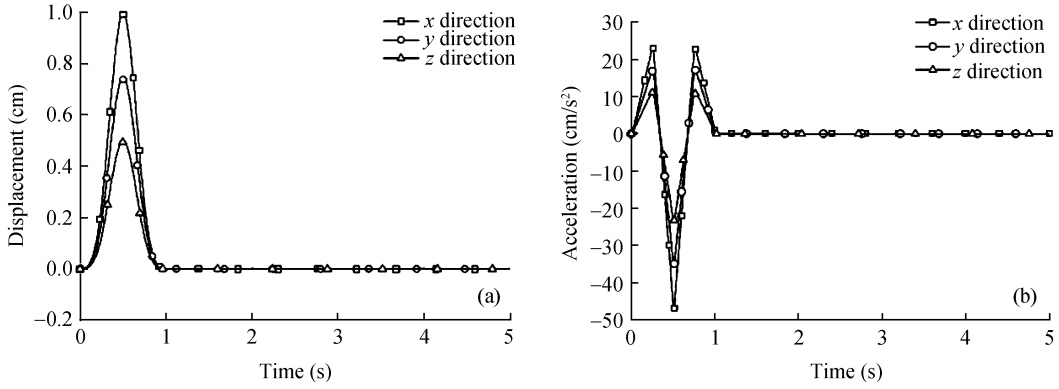

Figure 2 Time histories of incident waves for square foundation. (a) Displacement; (b) acceleration.

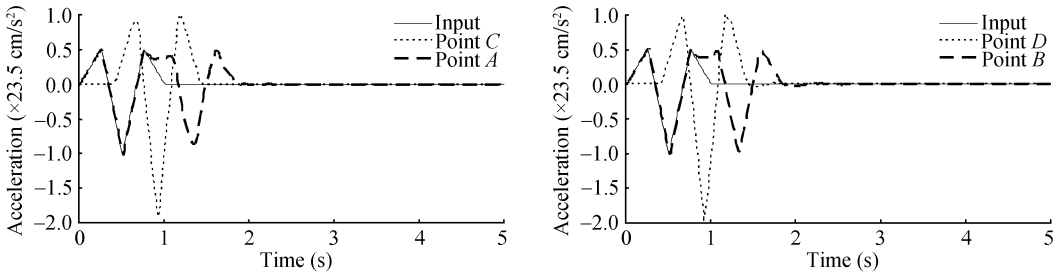

Figure 3 Time histories of acceleration responses at free surface (normalized amplitude) in z direction.

When the waves reach the free surface, they are reflected to the bottom. It also shows that reflected motions at the bottom points A and B can be seen and then are completely absorbed by the viscous-spring boundary leading nothing in response at points C and D after about 2 seconds. The peak accelerations at the corner point D on the free surface are exactly double of the input pulses, while a little less than double values are observed at the center point C. This is due to the filtering effects of the FE discretized system, as shown by the response spectra in Figure 4, where the original high frequency peaks of the input are cut off. Comparing Figure 4(a) and (b), it is evident that the fine mesh can efficiently reduce the cut-off of the high frequency peaks. In reality, this cut-off of the high frequency peaks only has little effects on structural response. The results of the example demonstrate that the viscous-spring boundary input model is capable of reproducing the free field motions and thus has sufficient accuracy for seismic analysis of mass infinite foundations.

For further verification of accuracy of the viscous-spring boundary model, a wave scattering effect due to semi-spherical cavity subjected to vertical harmonic P wave incident is analyzed. Since this problem is a symmetrical problem, only 1/4 spherical cavity is considered. As shown in Figure 5, the semi-spherical cavity with radius, R_0, contains an extension region, $l_0=2R_0$. The material properties are selected as shear modulus $G=8.4\times10^9$ Pa, mass density $\rho=2400$ kg/m^3 and Poison's ratio $\nu=0.25$. Dimensionless frequency, $a_0=R_0\omega/\pi c_P$ (c_P denotes the velocity of P wave), is selected as 0.25 and 0.50. The results are shown in Figure 6 and compared with that obtained by Sánchez-Sesma[24]. The response obtained by the viscous-spring boundary within the spherical cavity region (where x/R_0 is less than 1.0) is close to the results from Sánchez-Sesma, but there are some differences beyond the cavity (where x/R_0 is larger than 1.0). Since the ground motions beyond the canyon have little effect on the seismic response of arch dams, the viscous-spring boundary model has sufficient accuracy for seismic analysis of arch dams. Also, it is found that a larger area extending from the cavity does not seem to improve the accuracy for the viscous-spring boundary model.

2.2 Modeling of contraction joint opening

The nonlinear response of high arch dams due to contraction joint opening and closing during earthquakes is significant. It is of importance to appropriately model this nonlinear behavior in seismic safety evaluation of arch dams. Herein, the contact model proposed by Bathe and Chaudhary[25] is improved by the authors by install-

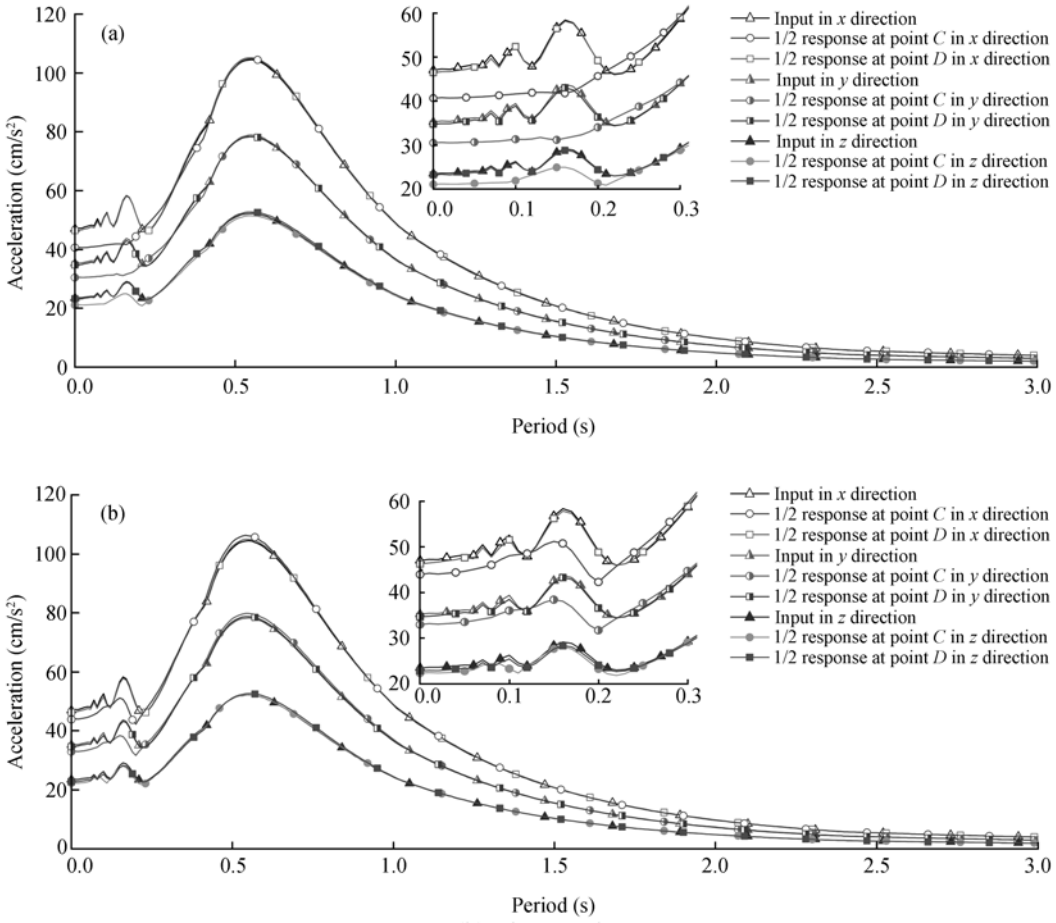

Figure 4 Acceleration response spectra at free surface. (a) Coarse mesh; (b) fine mesh.

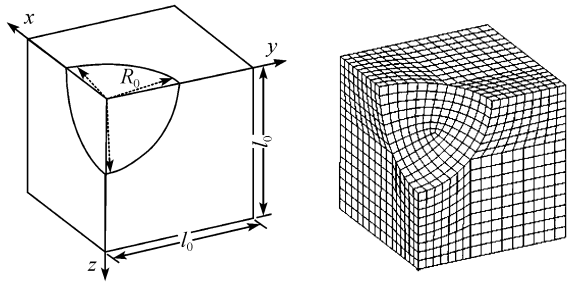

Figure 5 Geometry and FE mesh of 1/4 semi-spherical cavity.

ing shear springs to simulate keys to constrain tangential movement in contraction joints and is used in this study.

The contact boundary model consists of master and slave surfaces as shown in Figure 7(a). Each node on the slave surface is associated with a unique point on the master surface. The interaction between the slave and master surfaces is determined by the relation of the slave node and its corresponding master point as well as the pressure-overlap constitutive relation. Herein, the

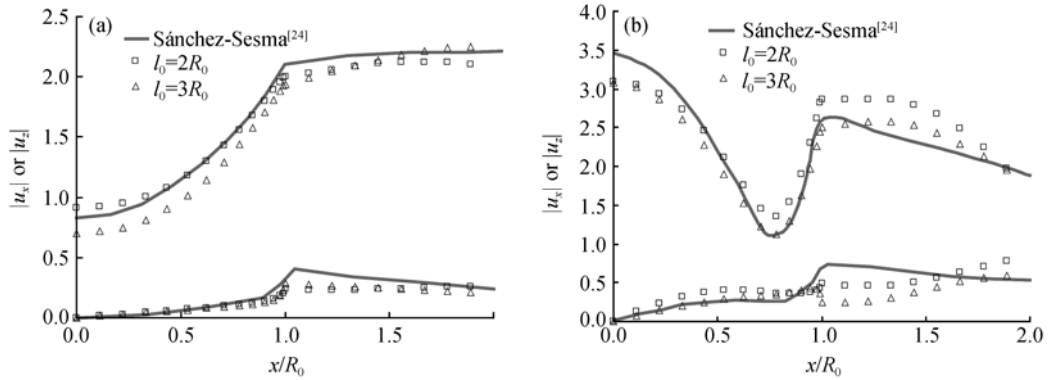

Figure 6 Surface amplitudes of vertical and horizontal displacements of semi-spherical cavity. (a) a_0=0.25; (b) a_0=0.50.

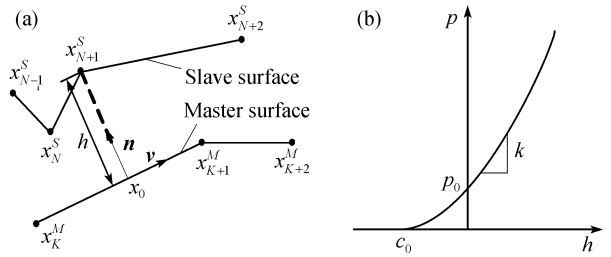

Figure 7 Contact boundary model for contraction joints. (a) Contact relation; (b) pressure-overlap constitutive relation.

exponential-type pressure-overlap constitutive relation (Figure 7(b)) is implemented into the model to prevent the slave node from overlapping the master surface. Details of the contact boundary model and the constitutive relations were discussed elsewhere[20,25].

The constitutive relations are

$$p=\begin{cases}0, & \text{for } h\leqslant c_0,\\ \dfrac{p_0}{(\exp(1)-1)}\left(\left(1-\dfrac{h}{c_0}\right)\left(\exp\left(1-\dfrac{h}{c_0}\right)-1\right)\right), & \text{for } h>c_0,\end{cases} \tag{6}$$

where c_0 is an initial overlap, and p_0 is the critical pressure value at zero overlap ($h=0$).

To simulate joint opening with perfect shear keys in arch dams, tangential springs with sufficiently large stiffness between monoliths are introduced in the contact boundary model to prevent shear slip from occurring.

2.3 Plastic-damage model for concrete

A simple plastic damage and thermodynamically consistent scalar degradation model proposed by Lee and Fenves[18] is introduced to simulate the damage-cracking of arch dams subjected to strong earthquakes. The main ingredients of the model are introduced here, a full description can be found in ref. [18].

In the plastic-damage model, the stress is factorized into two parts, one is stiffness degradation and the other is effective stress, and has the form

$$\boldsymbol{\sigma}=(1-\mathrm{d}(\bar{\boldsymbol{\sigma}},\boldsymbol{\varepsilon}^{\mathrm{p}}))\bar{\boldsymbol{\sigma}}=(1-\mathrm{d}(\bar{\boldsymbol{\sigma}},\boldsymbol{\varepsilon}^{\mathrm{p}}))\boldsymbol{E}_0:(\boldsymbol{\varepsilon}-\boldsymbol{\varepsilon}^{\mathrm{p}}), \tag{7}$$

where $\bar{\boldsymbol{\sigma}}$ is the effective stress; $\boldsymbol{E}_0$ is the initial elastic stiffness; $\mathrm{d}(\bar{\boldsymbol{\sigma}},\boldsymbol{\varepsilon}^{\mathrm{p}})$ denotes the scalar stiffness degradation variable, which can take values in the range from zero, for undamaged material with elastic behavior, to one, for fully damaged material; $\boldsymbol{\varepsilon}$ and $\boldsymbol{\varepsilon}^{\mathrm{p}}$ are the total strain and the plastic part of the strain, respectively.

The plastic strain rate is evaluated by the flow rule, which is governed by a scalar plastic flow potential function, G. The plastic potential is defined in the effective stress space, and the plastic strain rate is given by

$$\dot{\boldsymbol{\varepsilon}}^{\mathrm{p}}=\dot{\lambda}\frac{\partial G(\bar{\boldsymbol{\sigma}})}{\partial\bar{\boldsymbol{\sigma}}}, \tag{8}$$

where $\dot{\lambda}$ is the nonnegative plastic multiplier. For frictional material, such as concrete, a non-associated flow rule is introduced to obtain the proper dilatancy. A Drucker-Prager hyperbolic function which is continuous and smooth to ensure the unique flow direction is chosen in the model.

The yield function based on the one isotropic damage variable model proposed by Lubliner et al.[17] was modified by Lee and Fenves[18]. It includes two independent variables considering different evolution of strength under tension and compression. In terms of effective stresses the yield function takes the form

$$F(\bar{\boldsymbol{\sigma}},\tilde{\varepsilon}^{\mathrm{p}})=\frac{1}{1-\alpha}\Big[\alpha\boldsymbol{I}_1+\sqrt{3\boldsymbol{J}_2}+\beta(\tilde{\varepsilon}^{\mathrm{p}})\langle\hat{\sigma}_{\max}\rangle -\gamma\langle-\hat{\sigma}_{\max}\rangle\Big]-c_{\mathrm{c}}(\tilde{\varepsilon}^{\mathrm{p}}), \tag{9}$$

where

$\boldsymbol{I}_1=\mathrm{tr}(\bar{\boldsymbol{\sigma}})$ is the first invariant of effective stress tensor $\bar{\boldsymbol{\sigma}}$;

$\boldsymbol{J}_2=1/2\boldsymbol{s}$, $\boldsymbol{s}$ is the second invariant of deviatoric effect stress tensor;

$\tilde{\varepsilon}^{\mathrm{p}}$ is the equivalent plastic strain;

$\hat{\sigma}_{\max}$ denotes the algebraically maximum eigenvalue of $\bar{\boldsymbol{\sigma}}$, i.e. the first principle stress;

α is a coefficient which is evaluated by the initial shape of the yield function; it can be determined from the initial equibiaxial and uniaxial compressive yield stresses, σ_{b0} and σ_{c0}, as $\alpha=(\sigma_{\mathrm{b0}}-\sigma_{\mathrm{c0}})/(2\sigma_{\mathrm{b0}}-\sigma_{\mathrm{c0}})$;

γ is a dimensionless material constant; it enters the yield function only for stress states of triaxial compression;

$c_{\mathrm{c}}(\tilde{\varepsilon}^{\mathrm{p}})$ is the compressive cohesion stresses;

$\beta(\tilde{\varepsilon}^{\mathrm{p}})$ is a function defined as

$$\beta(\tilde{\varepsilon}^{\mathrm{p}})=\frac{c_{\mathrm{c}}(\tilde{\varepsilon}^{\mathrm{p}})}{c_{\mathrm{t}}(\tilde{\varepsilon}^{\mathrm{p}})}(1-\alpha)-(1+\alpha), \tag{10}$$

where $c_{\mathrm{t}}(\tilde{\varepsilon}^{\mathrm{p}})$ is the tensile cohesion stresses.

The dam safety is controlled by the tensile stresses during earthquakes, while compressive stresses usually do not approach the compressive strength of concrete in most cases. Consequently, for simplification, only the tensile damage of concrete is considered in this study.

The tensile damage state is characterized by the hardening variable, $\tilde{\varepsilon}_{\mathrm{t}}^{\mathrm{p}}$, which is referred to as equivalent plastic tension strain. The evolution equation for the damage variable is expressed as

$$\dot{\tilde{\varepsilon}}_{\mathrm{t}}^{\mathrm{p}} = r(\hat{\bar{\sigma}}) \cdot \dot{\hat{\varepsilon}}_{1}^{\mathrm{p}}, \tag{11}$$

where $\dot{\hat{\varepsilon}}_{1}^{\mathrm{p}}$ is the maximum plastic strain rate; and

$$r(\hat{\bar{\sigma}}) = \frac{\sum_{i=1}^{3} \left\langle \hat{\bar{\sigma}}_i \right\rangle}{\sum_{i=1}^{3} \left| \hat{\bar{\sigma}}_i \right|}, \ 0 \leqslant r(\hat{\bar{\sigma}}) \leqslant 1, \tag{12}$$

the Macauley bracket $\langle \bullet \rangle$ is defined by $\langle x \rangle = 0.5(|x|+x)$.

The mechanism of stiffness degradation under cyclic loading conditions is very complex, involving the opening and closing of microcracks, as well as their interaction. Considering the constitutive relation with linear strain-softening of concrete shown in Figure 8, compressive stiffness is recovered upon cracks closure as the load changes from tension to compression, while there is no tensile stiffness recovery as the load changes from compression to tension.

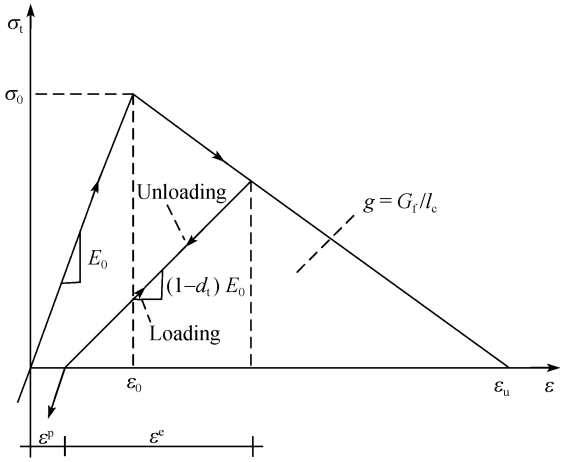

Figure 8 Response of concrete to cyclic loading.

The plastic-damage model is closely related to the dissipated fracture energy, which is defined as the energy required to form a unit area of crack. To eliminate the mesh-sensitivity in FE method, Lubliner et al.[17] and Lee and Fenves[18] assumed that the area under the $\sigma - \varepsilon^{\mathrm{p}}$ curve is equal to g, such that

$$g = \frac{G_{\mathrm{f}}}{l_{\mathrm{c}}}, \tag{13}$$

where G_{f} is the fracture energy of the concrete; l_{c} is the characteristic length related to the mesh size.

The stress-strain relationship satisfies that the fracture energy required to form a unit area crack is unique. Then the maximal strain is obtained as

$$\varepsilon_{\mathrm{u}} = \frac{2g}{\sigma_0} = \frac{2G_{\mathrm{f}}}{\sigma_0 l_{\mathrm{c}}}, \tag{14}$$

where σ_0 is uniaxial tensile strength of concrete. The stress–strain relationship used in the analysis is determined by the values of the fracture energy, uniaxial tensile strength and initial elastic stiffness, as well as the characteristic length, l_{c}.

3 Seismic damage-cracking analysis of Dagangshan arch dam

The 210 m high Dagangshan arch dam is under construction in the Dadu River of Southwest China. The normal water depth in upstream of the dam is designed as 195 m, and the depth of sedimentation during operation is assumed to be 125 m. This dam is being built in an extremely strong earthquake region with the design peak ground acceleration PGA=0.557 g. Safety evaluation of the dam subjected to the design earthquake is a crucial factor for the project. By combining the aforementioned models, the dynamic response of the dam is analyzed considering damage-cracking of dam concrete with 28 contraction joints. Massless foundation input model and viscous-spring boundary model are employed and compared.

3.1 Material parameters and loading conditions

The material parameters adopted in the analysis are shown in Table 1. The values of parameters are obtained from material tests carried out by Institute of Chengdu Hydroelectric Investigation & Design, except those of fracture energy, G_{f}, and damping ratio, ξ. An estimated value of 350 N/m is assumed for fracture energy in this

Table 1 Material properties of Dagangshan arch dam

	Elastic modulus (MPa)	Tensile strength (MPa)	Poisson ratio v	Fracture energy (N/m)	Unit weight (kN/m^3)
Concrete	3.12×10^4	3.25	0.17	325	24.0
Rock	1.885×10^4	-	0.258	-	26.5

study. The material damping ratio is considered via Rayleigh damping assumption.

The extreme loadings including the normal static and design earthquake loads are considered. The normal static loads include the dam gravity, upstream water loads, silt pressures, and design temperatures. The dynamic loads include design earthquake in three directions with the peak ground acceleration (PGA) of 0.557 g in the stream and cross-stream directions, and 0.371 g in the vertical direction. The time histories of the design earthquake are produced from the design response spectra (Figure 9). The hydrodynamic interaction is modeled via the added mass assumption, based on the finite element method with incompressible reservoir fluid

3.2 Finite element discretization

From the results of linear elastic material analysis, the tensile stresses at the upper portion of the dam far exceed the concrete tensile strength. Besides, due to the problem of stress concentration and element distortion, the tensile stresses at the upstream heel and near the dam-abutment interface are also larger than the tensile strength of concrete. The problem of stress concentration at the upstream heel of the dam is beyond the topic of current study and is not considered herein.

As shown in Figure 10, 8-node-brick elements with 2×2×2 Gauss integration are applied in the finite element discretization of the dam-foundation system. Densified element mesh discretization of about 2 m is adopted in the upper portion where the tensile stresses may exceed the tensile strength of concrete and damage-cracking is expected in this region. The densified element size is used for calculation of the characteristic length l_c compatible with the constitutive relation of concrete[13].

The plastic-damage model is adopted for the region with densified mesh. The material in the region with coarse mesh of the dam and the foundation rock is considered as linear elastic.

3.3 Results of damage cracking analysis

The case study includes using two seismic input models, i.e. massless foundation input model and viscous-spring boundary model. Different structural damping ratios of 0.05, 0.10, 0.12 and 0.15 for massless foundation input model and 0.05 for viscous-spring boundary model are assumed and compared.

The distributions of damage variable, i.e. stiffness degradation, d, of the dam are shown in Figures 11 and 12. It can be found that the most severely damaged region is in the upper portion of the dam, where, the cracks penetrate the whole section of the dam with a maximum damage variable, d_{max}, of 0.9 when using the massless foundation input model. However, when the viscous-spring boundary model considering radiation damping is employed, the damage region is limited to a

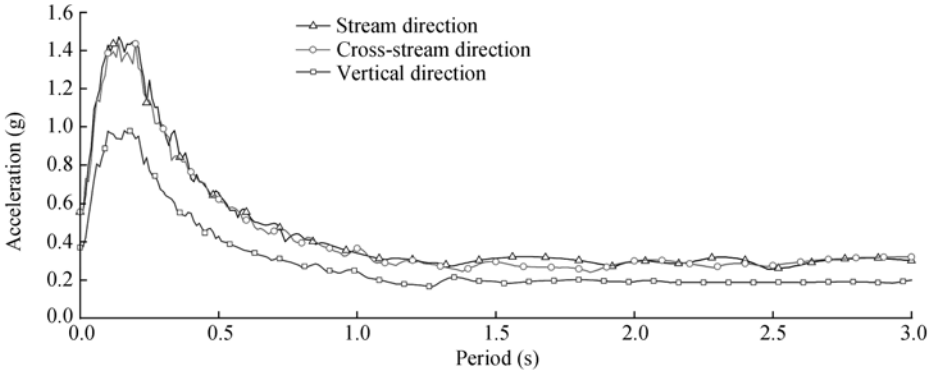

Figure 9 Design acceleration response spectra.

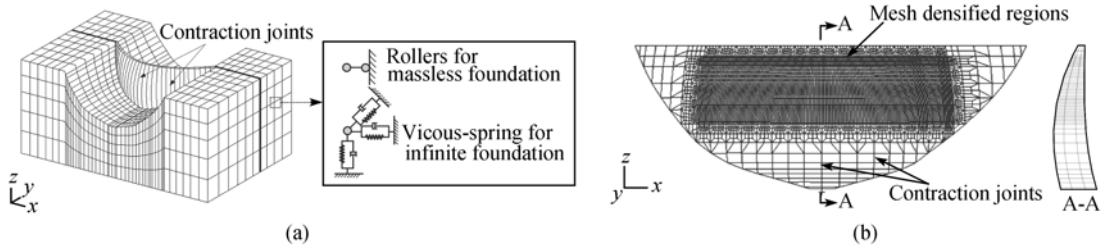

Figure 10 FE discretization of Dagangshan arch dam. (a) Dam-foundation system; (b) arch dam FE mesh.

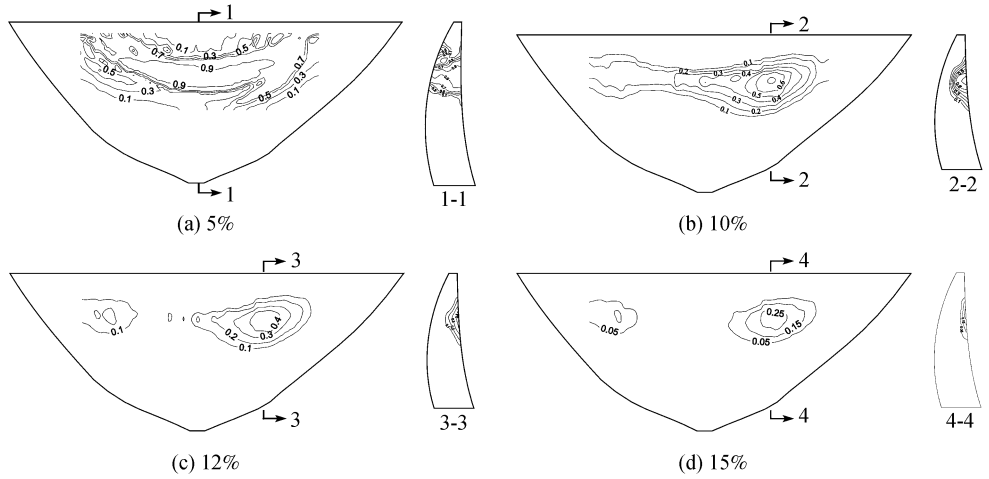

Figure 11 Distributions of damage variable d of the dam by massless foundation input model with different structural damping ratios.

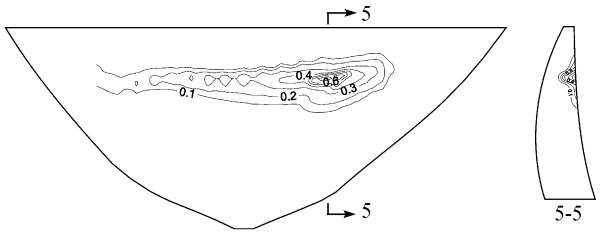

Figure 12 Distributions of damage variable d of the dam by viscous-spring boundary model with a 5% structural damping ratio.

localized area near the down-stream face of the dam, and the maximum damage variable, d_{max}, is also greatly reduced to 0.6. Interestingly, the damage variable contours obtained from massless foundation input model with an artificially increased value of about 10% structural damping ratio are close to that obtained from viscous-spring boundary model. When increasing the structural damping ratio to 15%, the damage region may further reduced and become smaller than that from the viscous-spring boundary model.

The comparison of crest displacements and joint openings are shown in Figures 13 to 15. In all cases, the damage cracking model with massless foundation input using a 5% structural damping ratio gives the maximum response envelop of displacements with a peak value of

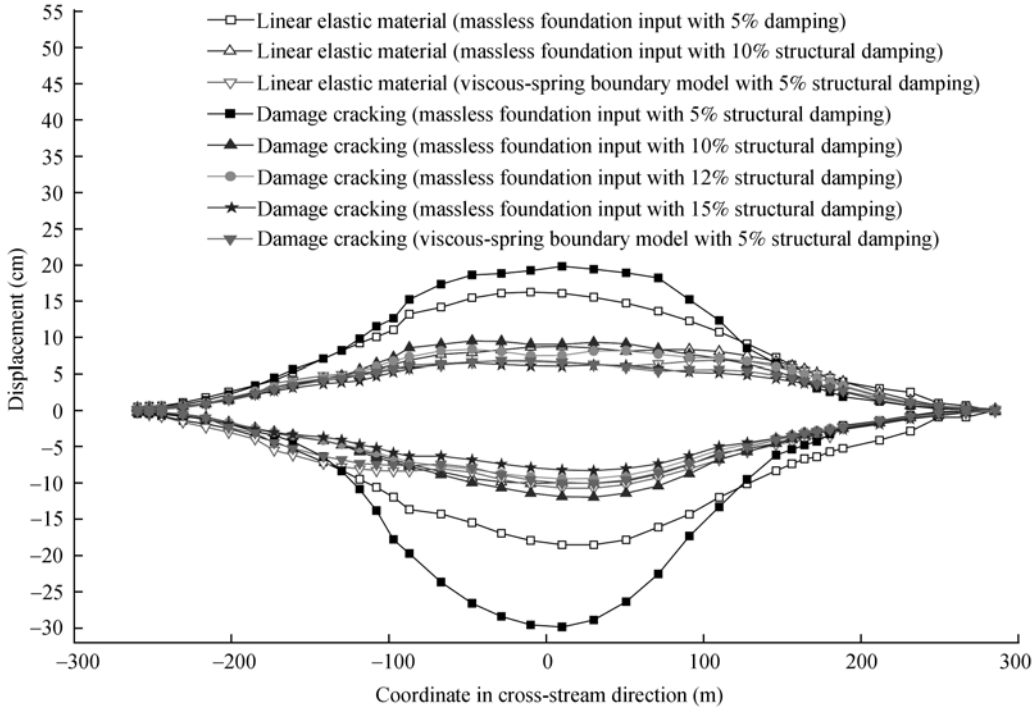

Figure 13 Envelope curve of peak displacement along crest.

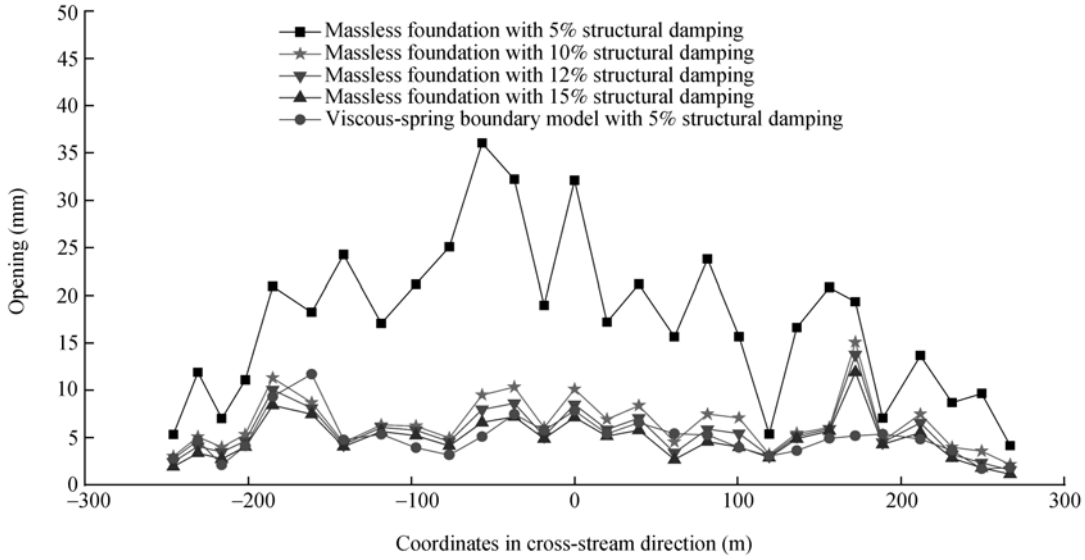

Figure 14 Comparison of joint openings by the damage-cracking model with different damping ratios and input models.

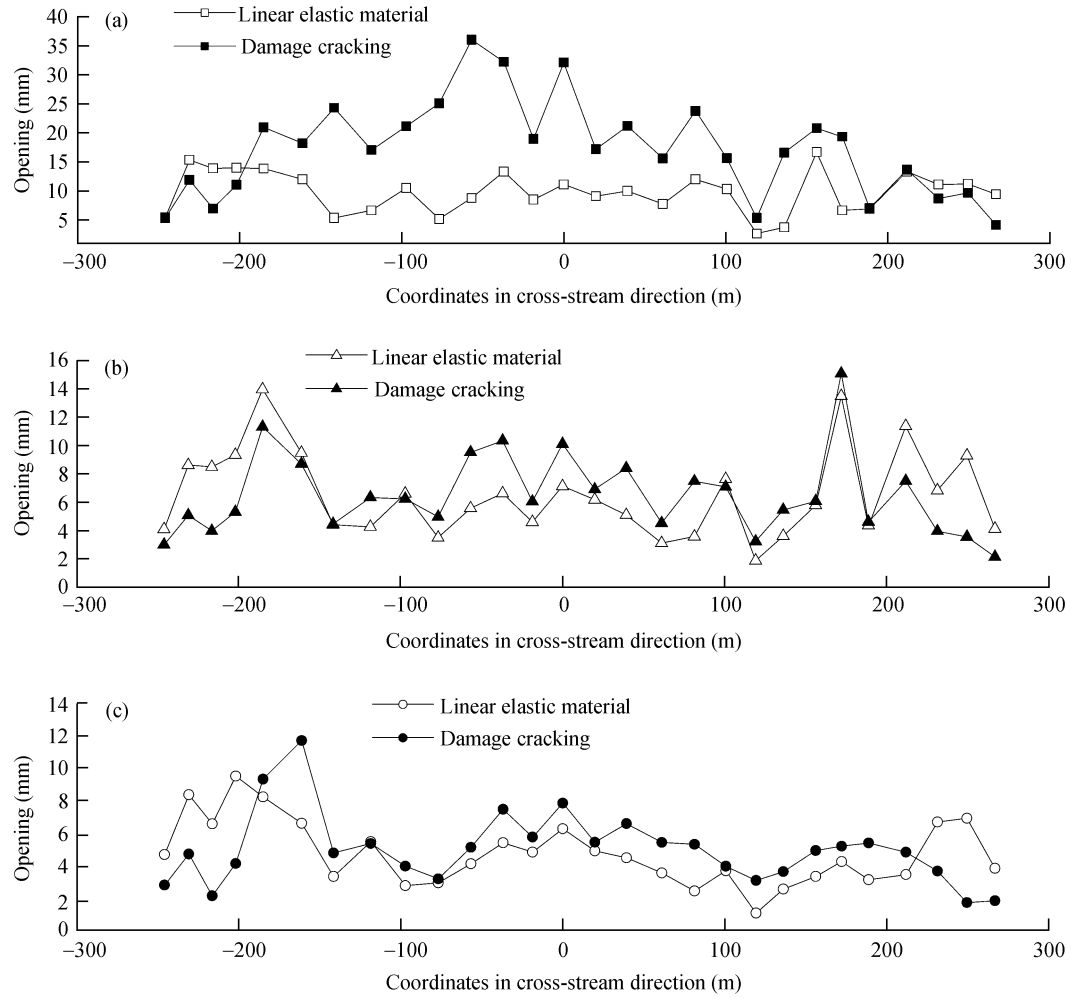

Figure 15 Comparison of joint opening by linear elastic material and damage-cracking model. (a) Massless foundation input with 5% structural damping; (b) massless foundation input with 10% structural damping; (c) viscous-spring boundary model with 5% structural damping.

30 cm toward upstream and the maximum joint opening of 36 mm from Figures 13 and 14. When using massless foundation input model with a 10%－15% structural damping ratio, the crest displacements and joint openings are greatly reduced and close to that from viscous-spring boundary model. From Figures 13 and 15(a), great difference of the displacements and joint openings are observed between the two material models when using massless foundation input with a 5% structural damping ratio, due to the significant degradation of structural stiffness in the upper portion of the dam. However, as shown in Figure 15(b) and (c) by considering the radiation damping effects or by increasing the structural damping ratio to about 10% for massless foundation, the effects of different material models on the displacement and joint opening responses become much smaller. Noticeably, in this case, the joint openings at the central portion of the dam by the damage model are still larger than that by the linear elastic model, while the joint openings at the quarter or side portion of the dam behave as an opposite tendency due to different capability of load transfer in arch direction between the two material models.

4 Conclusions

A comprehensive and nonlinear model consisting of a plastic-damage constitutive relation for concrete and a contact boundary simulation for contraction joints is presented for seismic damage-cracking analysis of arch dam-canyons. Two earthquake input procedures, i.e. the massless foundation and the viscous-spring boundary input models are employed for comparing the effects of different seismic input mechanisms and radiation damping. For examining whether there is a relatively higher structural damping ratio that may approximately imply the radiation damping of infinite canyons, several cases for the Dagangshan arch dam under the design earthquake are performed by massless foundation model with damping ratios of 5%, 10%, 12% and 15% for dam, and a structural damping ratio of 5% for viscous-spring boundary model. Findings from the analysis are as follows.

(1) Significant differences in response of contraction joint opening and damage-cracking development are observed between the massless foundation and viscous-spring boundary input models when both using the conventional value of damping ratio of 5% for dam. In this case, the maximum damage variable, $d_{\max}$, is greatly reduced from 0.9 to 0.6 when the radiation damping is considered. Also, the maximum joint opening is decreased from 36 to 12 mm.

(2) When the structural damping ratio is increased to 10%－15% using massless foundation, the crest displacements, contraction joint openings and damage-cracking in the dam are comparable to the results obtained by using viscous-spring boundary to take into account the radiation damping. However, for general situation of dam-canyon and ground motion, further investigation is necessary to examine whether a quantitative relationship exists between the equivalent increased value of structural damping for massless foundation model and the radiation effects of the infinite canyon in numerical simulation of arch dam-foundations.

Sincere thanks go to Profs. WANG GuangLun and JIN Feng for their suggestions. Ms. SHAO JingDong is also acknowledged for her assistance in the Dagangshan project study.

1 Zhang C H. Challenges of high dam construction to computational mechanics. 6th WCCM, Beijing, 2004
2 Clough R W. Non-linear mechanisms in the seismic response of arch dams. Proc Int Res Conf Earthquake Eng, Skopje, 1980. 669－684
3 Fenves G L, Mojtahedi S, Reimer R B. ADAP88: a computer program for nonlinear earthquake analysis of concrete arch dams. Report No. EERC 89-12, Earthquake Engineering Research Center. Berkeley: University of California, 1989
4 Fenves G L, Mojtahedi S, Reimer R B. Effect of contraction joints on earthquake response of an arch dam. J Struct Eng (ASCE), 1992, 118(4): 1039－1055
5 Zhang C H, Xu Y J, Jin F. Effects of Soil-Structure Interaction on Nonlinear Response of Arch Dams. Beijing: International Academic Publishers, 1997. 95－114
6 Zhang C H, Xu Y J, Wang G L, et al. Non-linear seismic response of arch dams with contraction joint opening and joint reinforcements. Earthq Eng Struct Dyn, 2000, 29(7): 1547－1566
7 Chen H Q. Model test and program verification on dynamic behavior of arch dam with contraction joints. Report No. SVL-94/2 IWHR, 1994
8 Lin G, Hu Z Q. Earthquake safety assessment of concrete arch and gravity dams. Earthq Eng Eng Vibration, 2005, 4(2): 251－264
9 Du X L, Tu J. Nonlinear seismic response analysis of arch dam-foundation systems-part II opening and closing contact joints. Bull Earthq Eng, 2007, 5(1): 121－133
10 Ayari M L, Saouma V E. A fracture mechanics based seismic analysis of concrete gravity dams using discrete cracks. Eng Fract Mech, 1990, 35(3): 587－598

11 Pekau O A, Zhang C H, Feng L M. Seismic fracture analysis of concrete gravity dams. Earthq Eng Struct Dyn, 1991, 20(2): 335－354
12 El-Aidi B, Hall J F. Nonlinear earthquake response of concrete gravity dams, part I: modeling. Earthq Eng Struct Dyn, 1989, 18(4): 837－851
13 Bazant Z P, Oh B H. Crack band theory for fracture of concrete. Mat Struct, 1983, 16(93): 155－177
14 Bhattacharjee S S, Léger P. Seismic cracking and energy dissipation in concrete gravity dams. Earthq Eng Struct Dyn, 1993, 22(4): 991－1007
15 Wang G L, Pekau O A, Zhang C H, et al. Seismic fracture analysis of concrete gravity dams based on nonlinear fracture mechanics. Eng Fract Mech, 2000, 65(1): 67－87
16 Cervera M, Oliver J, Faria R. Seismic evaluation of concrete dams via continuum damage models. Earthq Eng Struct Dyn, 1995, 24(6): 1225－1245
17 Lubliner J, Oliver J, Oller S, et al. A plastic-damage model for concrete. Int J Solids Struct, 1989, 25(3): 299－326
18 Lee J, Fenves L G. Plastic-damage model for cyclic loading of concrete structures. J Eng Mech (ASCE), 1998, 124(3): 892－900
19 Lee J, Fenves L G. A plastic-damage concrete model for earthquake analysis of dams. Earthquake Eng Struct Dyn, 1998, 27(9): 937－956
20 Lysmer J, Kuhlemeyer R L. Finite dynamic model for infinite media. J Eng Mech Division (ASCE), 1969, 95(3): 759－877
21 Liao Z P, Wong H L, Yang B P, et al. A transmitting boundary for transient wave analyses. Scientia Sinica (Ser A), 1984, 27(10): 1063－1076
22 Deeks A J, Randolph M F. Axisymmetric time-domain transmitting boundary. J Eng Mech (ASCE), 1994, 120(1): 25－42
23 Liu J B, Lu Y D. A direct method for analysis of dynamic soil-structure interaction based on interface idea. In: Zhang C H, Wolf J P, eds. Dynamic Soil-Structure Interaction－Current Research in China and Switzerland. Beijing: International Academic Publishers, 1997. 258－273
24 Sánchez-Sesma F J. Diffraction of elastic waves by three-dimensional surface irregularities. Bull Seism Soc Am, 1983, 73(8): 1621－1636
25 Bathe K J, Chaudhary A. A solution method for planar and axisymmetric contact problems. Int J Numer Methods Eng, 1985, 21(1): 65－88